Diffraction studies for stoichiometry effects in $BaTiO_3$ grown by molecular beam epitaxy on Ge(001)

Min-Hsiang Mark Hsu, Clement Merckling, Salim El Kazzi, Marianna Pantouvaki, Oliver Richard, Hugo Bender, Johan Meersschaut, Joris Van Campenhout, Philippe Absil, and Dries Van Thourhout

Citation: J. Appl. Phys. **120**, 225114 (2016); doi: 10.1063/1.4972101
View online: http://dx.doi.org/10.1063/1.4972101
View Table of Contents: http://aip.scitation.org/toc/jap/120/22
Published by the American Institute of Physics

Diffraction studies for stoichiometry effects in $BaTiO_3$ grown by molecular beam epitaxy on Ge(001)

Min-Hsiang Mark Hsu,[1,2,a)] Clement Merckling,[1] Salim El Kazzi,[1] Marianna Pantouvaki,[1] Oliver Richard,[1] Hugo Bender,[1] Johan Meersschaut,[1] Joris Van Campenhout,[1] Philippe Absil,[1] and Dries Van Thourhout[2,3]
[1]*imec, Kapeldreef 75, 3001 Leuven, Belgium*
[2]*Photonics Research Group, INTEC, Ghent University—imec, Technologiepark-Zwijnaarde 15, Ghent 9052, Belgium*
[3]*Center for Nano- and Biophotonics (NB-Photonics), Ghent University, Technologiepark-Zwijnaarde 15, Ghent 9052, Belgium*

(Received 17 August 2016; accepted 29 November 2016; published online 15 December 2016)

In this work, we present a systematic study of the effect of the stoichiometry of $BaTiO_3$ (BTO) films grown on the Ge(001) substrate by molecular-beam-epitaxy using different characterization methods relying on beam diffraction, including reflection high-energy electron diffraction (RHEED), X-ray diffraction (XRD), and selected-area electron diffraction in transmission electron microscopy. Surprisingly, over a wide range of [Ba]/[Ti] ratios, as measured by the Rutherford backscattering spectrometry, all the BTO layers exhibit the same epitaxial relationship $\langle 100\rangle$BTO(001)// $\langle 110\rangle$Ge(001) with the substrate, describing a 45° lattice rotation of the BTO lattice with respect to the Ge lattice. However, varying the [Ba]/[Ti] ratio does change the diffraction behavior. From RHEED patterns, we can derive that excessive [Ba] and [Ti] generate twinning planes and a rougher surface in the non-stoichiometric BTO layers. XRD allows us to follow the evolution of the lattice constants as a function of the [Ba]/[Ti] ratio, providing an option for tuning the tetragonality of the BTO layer. In addition, we found that the intensity ratio of the 3 lowest-order Bragg peaks $I_{(001)}/I_{(002)}$, $I_{(101)}/I_{(002)}$, and $I_{(111)}/I_{(002)}$ derived from $\omega - 2\theta$ scans characteristically depend on the BTO stoichiometry. To explain the relation between observed diffraction patterns and the stoichiometry of the BTO films, we propose a model based on diffraction theory explaining how excess [Ba] or [Ti] in the layer influences the diffraction response. *Published by AIP Publishing.*
[http://dx.doi.org/10.1063/1.4972101]

I. INTRODUCTION

Given the unique physical properties of thin-film perovskite oxides (ABO_3), exhibiting at the same time strong ferroelectric, piezo-electric, and electro-optical effects, their monolithic integration with compound semiconductors offers many new degrees of freedom for advanced device generations.[1–3] It is widely reported that the above-mentioned effects are superior in single crystalline ABO_3 compared to any other crystal type.[4–6] However, obtaining high-quality integration of crystalline ABO_3 with semiconductors remains challenging due to the huge discrepancy in their respective crystal lattices and chemical properties.[5,6]

The path towards the integration of crystalline ABO_3 thin films with semiconductors was not opened until the late 1990s. McKee *et al*. utilized an alkaline earth metal submonolayer to achieve high quality $SrTiO_3$ (STO) epitaxy on Si by molecular beam epitaxy (MBE).[7] Since then, the epitaxy of STO onto Si substrates was heavily investigated, given its excellent compatibility with several other functional oxides and its interesting material characteristics.[8–10] Nevertheless, its properties are highly dependent on the exact epitaxial conditions such as substrates used, growth temperature, and, especially, stoichiometry.[11–14] Even if several techniques for realizing high quality STO thin film have been developed,[15–17] avoiding local or global non-stoichiometry is still difficult.[18] In order to well control material properties, it is important to develop an efficient method to understand the stoichiometry inside the layer during and after the growth. To evaluate the composition of the STO layer, several diffraction techniques are commonly applied.[19–21] During the growth, many groups utilize reflection high energy electron diffraction (RHEED) to monitor the Sr and Ti flux ratio ([Sr]/[Ti]) in the layer in real-time, and to control the composition.[19,20] After the growth, the out-of-plane lattice constants retrieved from a $\omega - 2\theta$ scan along the [001] axis in X-ray diffraction (XRD) can also qualitatively reveal the ratio [Sr]/[Ti].[19,21]

However, for other ABO_3 oxides, these are much less discussed than for STO. Even though all ABO_3 have a similar crystal structure, the different electron numbers, atom sizes, and composition from various elements will still lead to different diffraction behaviors.[22] Given its strong ferroelectric and electro-optical properties, lead-free $BaTiO_3$ (BTO) has been studied for over 70 years.[23,24] With the successful development of an STO on the Si epitaxial process, also BTO recently is getting considerable research interest, in particular, for the integration in novel Si-based devices. For example, the authors of Refs. 2 and 25 showed high speed silicon integrated modulators, exploiting the excellent electro-optical properties of a hybrid integrated BTO layer. However, as with STO, the characteristics of such BTO layers are greatly dependent on the [Ba]/[Ti]

a)Electronic mail: min.hsiang.hsu@imec.be

composition,[26–28] so accurately controlling the stoichiometry of the deposited BTO is crucial.

Therefore, in this work, we will mainly investigate the impact of the stoichiometry of an epitaxially grown BTO layer on its diffraction characteristics. The BTO layers are grown by MBE onto Ge(001), which has a quasi-zero lattice mismatch to BTO in a 45° crystal rotation epitaxial relationship.[29] First, the [Ba]/[Ti] ratio is measured by Rutherford backscattering spectroscopy (RBS). Then, the results of RHEED, XRD, and transmission electron microscope (TEM) experiments are systematically presented and discussed. Moreover, a model for the diffraction by non-stoichiometric BTO is developed, which explains several of the unique observations in our experiments.

II. EXPERIMENTS

Four samples with various [Ba]/[Ti] ratios and denoted A to D were prepared. All of them were grown on a 4-in. Ge(001) substrate in a Riber49 200 mm production MBE reactor. Ti metal is evaporated with an electron beam controlled by a feedback loop from a mass spectrometer to keep a constant flux during growth. The Ba atomic flux is obtained using a standard Knudsen effusion cell and the [Ba]/[Ti] flux ratio is tuned with the help of a quartz crystal microbalance. A remote plasma source is used to produce atomic oxygen during the growth.

Prior to BTO deposition, the Ge native oxide was thermally desorbed by heating the substrate to 800 °C for 30 min, resulting in a bright (2×1) RHEED reconstruction pattern. In order to accommodate both BTO and Ge lattices, a 45° rotation of the BTO lattice with respect to Ge substrate is required and is initiated via inserting a 0.5 monolayer BaO between BTO and Ge.[29] This BaO layer is realized by growing a 0.5 monolayer (ML) of Ba at 550 °C resulting in a 2×1 Ba-Ge(001) surface followed by oxygen exposure. The substrate temperature is then increased to 630 °C for BTO growth under an oxygen $\sim 1.6 \times 10^{-6}$ Torr partial pressure.

For all samples, [Ba] and [Ti] were measured by Rutherford backscattering spectrometry (RBS), and the results are summarized in Table I, where the [Ba] excess ε is defined by $Ba_{1+\varepsilon}TiO_{3-\zeta}$. The [Ba] excess in the BTO films varies from −90% to 28%. The 4 samples used in the present study are the representatives of each unique phenomenon which will be detailed in the following. XRD measurements show that above 28%, the films become completely amorphous and then are not included in the current study. In Section III, we provide and discuss the detailed structural and diffraction behavior as observed from RHEED, XRD, and TEM experiments as function of [Ba]/[Ti] for the different samples.

TABLE I. Summary of RBS-measured [Ba]/[Ti] ratio in the different BTO-layers grown.

	[Ba]/[Ti] in RBS	Excessive [Ba][a]
Sample A	0.10	−90%
Sample B	0.96	−4%
Sample C	1.08	+8%
Sample D	1.28	+28%

[a][Ba] excess, ε, is defined by $Ba_{1+\varepsilon}TiO_{3-\zeta}$.

III. RESULTS

Figure 1 presents the evolution of the RHEED diffraction patterns and the corresponding schematics for the samples A, B, C, and D. In Figure 1(a), sample A with −90% [Ba] excess in the BTO shows spotty RHEED patterns indicating 3D growth with rough surface. The corresponding miller-indexed planes can be defined from the tetragonal BTO crystal lattice. Given the excess [Ti], the oxygen content in the BTO is decreased, leading to both Ti-rich and oxygen-deficient BTO compounds, $BaTi_{1+\Delta}O_{3-\delta}$.[30] It has been reported that oxygen-deficient BTO contains $(111)_{BTO}$ twins,[31,32] which can be observed in the RHEED patterns along $[100]_{BTO}$ in Figure 1(a). With a [Ba]/[Ti] ratio closer to the stoichiometric composition, the RHEED patterns of sample B (4% extra [Ti]) change (Figure 1(b)): instead of a spot-only 3D pattern, they now show streak-lined patterns overlaid by few spots, representing the 2D layer with much improved roughness on the surface. Diffraction lines at (11), (-1-1), (01), and (0-1) can be observed revealing that the diffraction behavior is changed as the [Ba]/[Ti] ratio reaches unity. Figure 1(c) shows RHEED patterns of sample C which has 8% extra [Ba]. One can notice that the extra Ba roughens the surface again, resulting in more spotty patterns overlaid on the streak lines. In addition, there are extra spots between the diffraction lines along $[110]_{BTO}$ and $[100]_{BTO}$ directions, denoted by the gray ellipses in the schematic representations. With further increasing the [Ba] content to 28% in sample D, the spottier patterns, as presented in Figure 1(d), indicate the surface roughens further. In addition, more extra spots between the diffraction lines emerge, as gray labeled in the schematic. Those extra spots between the diffraction lines in Figures 1(c) and 1(d) originate from $(111)_{BTO}$ twins in the crystalline layer. In order to incorporate extra BaO in the Ba-rich BTO, $(111)_{BTO}$ nanotwins and $(001)_{BTO}$ Ruddlesden-Popper planar faults are usually generated.[19,32] Therefore, more [Ba] will induce more twins as observed in the RHEED patterns of Figures 1(c) and 1(d), respectively. Generally, none of the samples shows extra ×2 reconstruction lines in the RHEED pattern along $[110]_{BTO}$ and $[100]_{BTO}$ resulting from the BaO for the Ba-rich and TiO_2 for the Ti-rich BTO, respectively. This might be because the [Ba]/[Ti] element ratio is too far away from the stoichiometric condition to observe this extra ×2 reconstruction lines. On the other hand, even though this work covers a wide range of the [Ba]/[Ti] cation ratios for $Ba_{1+\varepsilon}TiO_{3-\zeta}$, the RHEED pattern evolutions with respect to stoichiometry shows similar behaviors already reported previously in the literature.[33,34]

Figure 2 describes a series of XRD scans for different BTO samples with using the 1° slit in front of the rocking-curve detector. Figure 2(a) presents the azimuthal ϕ scans for all four samples. While measuring $(\pm 1 \pm 11)_{BTO}$ in samples B to D, $(\pm 2 \pm 24)_{BTO}$ was measured for sample A indicating the absence of the $(\pm 1 \pm 11)_{BTO}$ in the latter. Despite large discrepancies in the [Ba]/[Ti] ratio, surprisingly, all

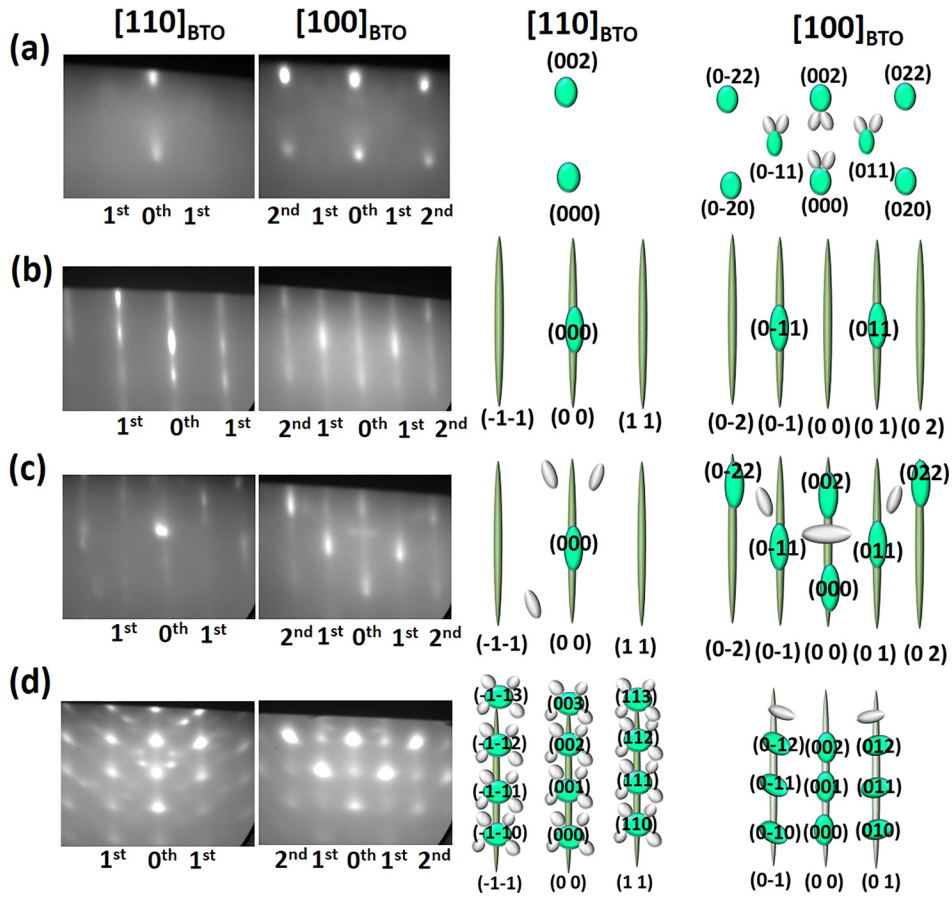

FIG. 1. The RHEED diffraction patterns and corresponding schematics along $[100]_{BTO}$ and $[110]_{BTO}$ of (a) sample A with 90% extra [Ti], (b) sample B with 4% extra [Ti], (c) sample C with 8% additional [Ba], and (d) sample D with 28% additional [Ba], respectively.

samples still exhibit the same epitaxial relationship with the Ge-substrate, $\langle 100\rangle$BTO(001)//$\langle 110\rangle$Ge(001), i.e., a 45° in-plane rotation of the BTO lattice with respect to the Ge lattice. Such 4-fold symmetry also corresponds with azimuthal RHEED scans for all the samples. The symmetrical $\omega - 2\theta$ scan along the $[001]_{BTO}$ direction shown in Figure 2(b) reveals that all BTO layers are seemingly single-crystalline, only showing $(001)_{BTO}$ Bragg reflection peaks. However, for sample A, the first-order Bragg peak, $(001)_{BTO}$, is missing. This, to some extent, agrees with the absence of some RHEED reflections in sample A, confirming the diffraction behavior changes due to the [Ti] excess. Also, an

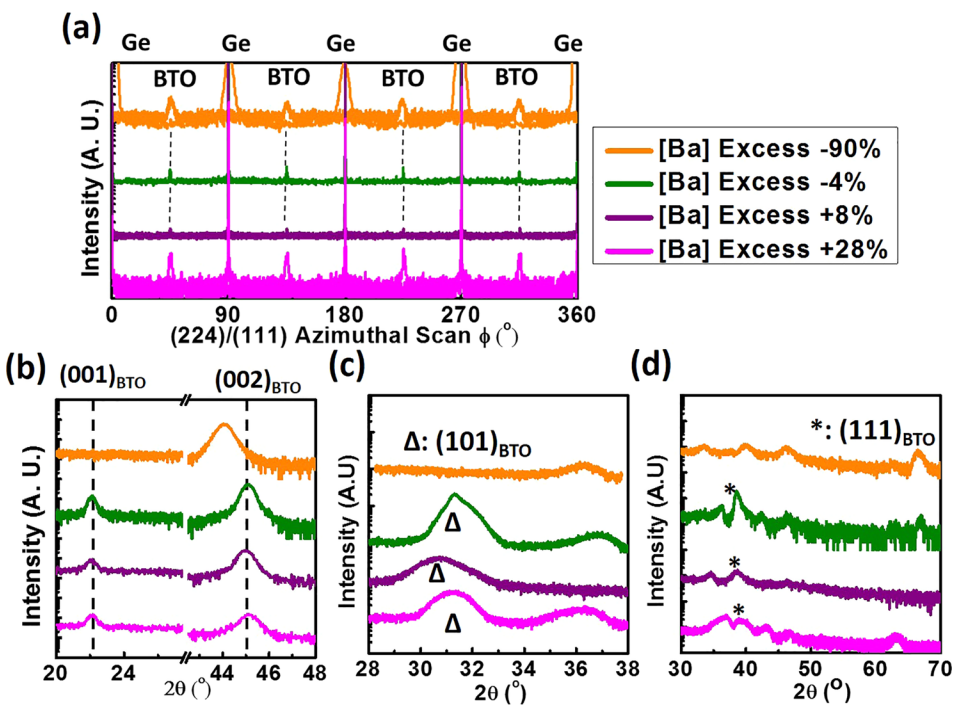

FIG. 2. (a) The azimuthal ϕ scan of $(\pm 1 \pm 11)_{BTO/Ge}$ for the samples B to D, and that of $(\pm 2 \pm 24)_{BTO/Ge}$ for the sample A. The $\omega - 2\theta$ scan along (b) $[001]_{BTO}$, (c) $[101]_{BTO}$, and (d) $[111]_{BTO}$ for all the samples.

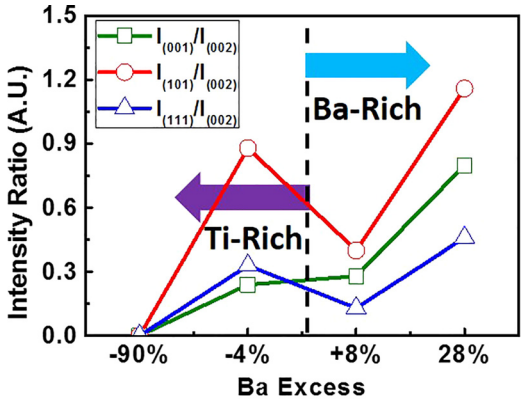

FIG. 3. The XRD intensity ratio of $(001)_{BTO}$, $(101)_{BTO}$, and $(111)_{BTO}$ to $(002)_{BTO}$ for all samples, evaluated from the $\omega-2\theta$ scans shown in Figure 2.

asymmetrical $\omega-2\theta$ scan along $[101]_{BTO}$ is conducted and shows a poly-crystalline diffraction spectrum with multiple peaks for all samples except for sample C. These multi-peaks can be filtered by using a narrower slit ($<1°$) in front of the XRD detector or using a detector in the triple-axis configuration. They result from the poly-crystalline and non-stoichiometric BaO and TiO_2 compounds contained in the films such as Ba_2TiO_4, $BaTi_2O_5$, $BaTi_4O_9$, etc.[28] The diffraction spectra for these compounds are too complicated to be resolved with our measurement setup.[35,36] Among the different peaks in the spectrum, the $(101)_{BTO}$ peak can be identified by ϕ-scan measurements: only the $(101)_{BTO}$ peak belonging to epitaxial BTO can show 4-fold symmetry as shown in Figure 2(a). From the ϕ-scan of $(101)_{BTO}$, we found that the $(101)_{BTO}$ is only in sample A not observable revealing the unique diffraction behavior triggered by extra [Ti]. Finally, Figure 2(d) shows the asymmetrical $\omega-2\theta$ scan along $[111]_{BTO}$. By measuring the ϕ-scan of $(111)_{BTO}$, this Bragg reflection does not appear for sample A suggesting again that the 90% excessive [Ti] induces different diffraction behaviors. Besides, all samples, including sample A, show a poly-crystalline diffraction spectrum, presenting even more peaks than for the scan along $[101]_{BTO}$. From this, we conclude the $\omega-2\theta$ scan along $[111]_{BTO}$ is a better measure for the assessment of the crystallinity of the ideal stoichiometric [Ba] = [Ti] BTO thin film. This correlates with the fact that the non-stoichiometric compounds tend to precipitate in the grain boundaries of twinned $(111)_{BTO}$.[37] Yet, it is important to realize that the general $\omega-2\theta$ scan along $[001]_{BTO}$ is not sufficient to determine the crystalline quality of the layer.

To understand the XRD diffraction behavior as function of the [Ba]/[Ti] ratio, the intensity ratio of the three lowest-ordered Bragg peaks ($(001)_{BTO}$, $(101)_{BTO}$, and $(111)_{BTO}$) relative to the $(002)_{BTO}$ peak is calculated and summarized in Figure 3. Note that only sample A does not show $(001)_{BTO}$, $(101)_{BTO}$, and $(111)_{BTO}$. We can observe that the ratio $I_{(001)}/I_{(002)}$ is increasing with increasing Ba-content in the BTO. On the other hand, $I_{(101)}/I_{(002)}$ and $I_{(111)}/I_{(002)}$ decrease when evolving from Ti-rich to Ba-rich BTO. When further increasing the [Ba] content, those ratios are increasing again, even above those obtained for sample B, which is closer to the ideal stoichiometric condition. We will discuss the observed variations and the relation to our model later in this paper.

From the symmetric and asymmetric $\omega-2\theta$ scans shown in Figure 2, the in-plane and out-of-plane lattice constants for sample B to sample D can be calculated. Yet, to determine the in-plane lattice constant of sample A, we have to rely on the $\omega-2\theta$ scan of $(224)_{BTO}$ (not shown here) because the $(101)_{BTO}$ and $(111)_{BTO}$ peaks are missing. The out-of-plane lattice constant, $a_\perp$, and the in-plane lattice constant, $a_\parallel$, are summarized in Figure 4(a). The local minimum for $a_\perp$ is obtained for the sample with [Ba]/[Ti] = 1, similar to what is observed for $a_\perp$ of STO. The in-plane lattice constant $a_\parallel$, on the other hand, decreases with increasing [Ba] content inside the layer. The trend for the lattice constants $a_\perp$ and $a_\parallel$ for excessive [Ti] can be explained by Coulomb repulsion induced by the extra [Ti]. Since the extra [Ti] induces oxygen vacancies V_o in the BTO to keep charge neutrality, the neighboring Ti-ions show charge repulsion due to the absence of oxygen atoms in the crystal. Therefore, excessive [Ti] will also result in an expansion of the crystal lattice. For sample C and sample D with excess [Ba], the out-of-plane lattice constant $a_\perp$ is seemingly independent of the [Ba] content. However, the in plane lattice constant $a_\parallel$ decreases as more [Ba] is incorporated inside the layer, probably related to the smaller lattice constants of Ba_2TiO_4.[36] Therefore, when evaluating the tetragonality ($a_\perp/a_\parallel$) to understand the BTO polarization in Figure 4(b), sample D with 28% [Ba] excess shows a dramatic increment, indicating strong out-of-plane polarization. All other samples show $a_\perp/a_\parallel$ below 1, indicating the in-plane polarization. This is believed to stem from the large mismatch in the thermal expansion coefficients of BTO ($\alpha_{BTO} = 1.1 \times 10^{-5}\,K^{-1}$) and Ge ($\alpha_{Ge} = 5.8 \times 10^{-6}\,K^{-1}$).[38,39] In order to qualitatively

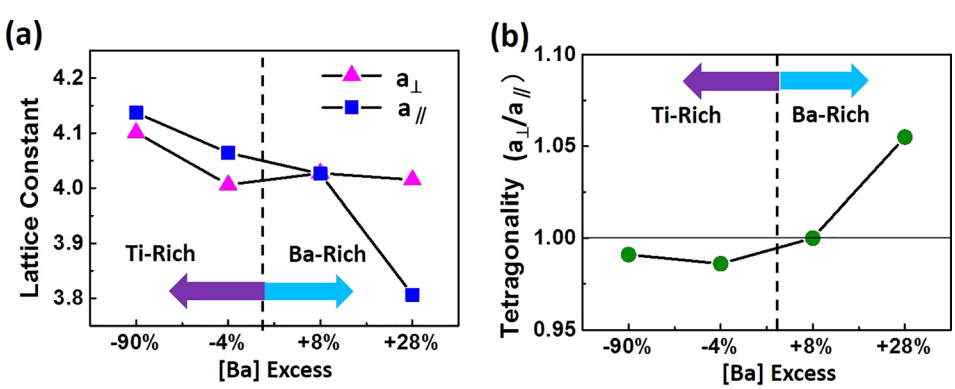

FIG. 4. (a) The in-plane ($a_\parallel$) and out-of-plane ($a_\perp$) lattice constants, derived from $\omega-2\theta$ scans shown in Figure 2. (b) The corresponding tetragonality ($a_\perp/a_\parallel$) for all samples.

explain this, we assume that, during the growth, the crystal lattice of BTO is matched to the Ge lattice. Hence, the lattice constant for BTO and Ge at the growth temperature of 630 °C can be written as $a^{630\,^{\circ}C}{}_{BTO\&Ge}$. When cooling down to 20 °C, the BTO and Ge lattice constants become $a^{20\,^{\circ}C}{}_{BTO} = a^{630\,^{\circ}C}{}_{BTO\&Ge}[1 + \alpha_{BTO}(20–630)]$ and $a^{20\,^{\circ}C}{}_{Ge} = a^{630\,^{\circ}C}{}_{BTO\&Ge}[1 + \alpha_{Ge}(20–630)]$, respectively. Consequently, since α_{BTO} is larger than α_{Ge}, the BTO layer will experience tensile strain from the Ge substrate driving the polarization to lie in the plane of the surface.[40] Summarizing, from our studies, the stoichiometry of the BTO-sample also provides a route to control its tetragonality, optimizing it for a given device application.[34,41]

Figure 5 presents the comparison of cross-sectional high resolution TEM (HRTEM) images with the corresponding selected area electron diffraction (SAED) images for samples A and B. The samples were prepared by taking a cross-section along the $[100]_{BTO}//[110]_{Ge}$ zone axis and the $[001]_{BTO}//[001]_{Ge}$ vertical direction. The black shadows in the HRTEM images are believed to originate either from the presence of defects or from roughness of the TEM sample lamella. The corresponding SAED Bragg peaks are defined based on the reference of the Ge substrate. In Figures 5(a) and 5(c), the HRTEM images for, respectively, samples A and B show a sharp BTO/Ge interface without the formation of amorphous GeO_x suboxides at the hetero-interfaces. Also, the bright SAED spots in both samples (Figures 5(b) and 5(d)) agree with the good crystallinity already deduced from the $\omega - 2\theta$ scan in Figure 2. However, compared to sample A, the SAED pattern for sample B shows more diffraction spots. It confirms that the 90% excessive [Ti] generates a change in the diffraction behavior, explaining the observed diffraction behavior of the different BTO layers. Given the resolution of the measurement, the difference between the lattice constants $a_{\perp}$ and $a_{\parallel}$ cannot be resolved from the SAED patterns though.

IV. DISCUSSION

To qualitatively understand the relation between the observed diffraction patterns and the ratio [Ba]/[Ti], we calculate the peak diffraction intensity and position corresponding to various planes simply based on diffraction theory without considering instrument geometry.[22] In the calculation, we assume the BTO structure is cubic for simplicity. The diffraction intensity can be described by the following formula:

$$I_{hkl} \propto \frac{\lambda^3 \times |F_{hkl}|^2 \times M \times L.P.}{V_c^2 \mu_\varrho}, \tag{1}$$

where λ is the beam wavelength, F_{hkl} is the structure factor of the miller-indexed (hkl) plane, M is the multiplicity of the (hkl) (in the cubic BTO system, M = 6 for {001} and {002}; M = 12 for {110}; and M = 8 for {111}), L.P. is the Lorentz-polarization factor, V_c is the BTO unit cell volume, and μ_ρ is the beam absorption in the layers. F_{hkl} and L.P are given by the following relations:

$$F_{hkl} = f_{Ti} + f_{Ba}(-1)^{h+k+l} + f_O[(-1)^{h+k} + (-1)^{k+l} + (-1)^{h+l}], \tag{2}$$

$$L.P. = \frac{(1 + \cos^2 2\theta_{hkl})}{\sin 2\theta_{hkl} \sin \theta_{hkl}}, \tag{3}$$

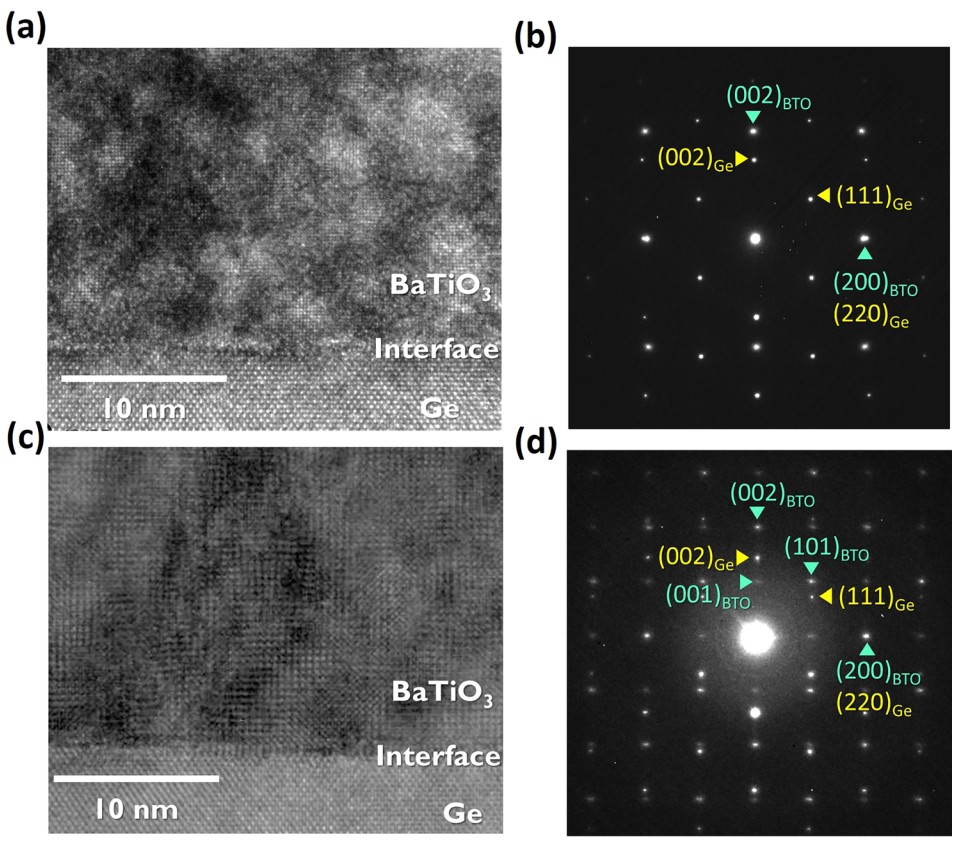

FIG. 5. (a) and (b) are HR-TEM and SAED images of sample A with 90% [Ti], respectively; (c) and (d) are those images for sample B with 4% extra [Ti]. The miller planes in the SAED images are indexed based on the tetragonal lattice system and Ge(001) reference.

where f_{Ti}, f_{Ba}, and f_O are the atomic form factors of Ti, Ba, and O, respectively, and θ_{hkl} is the Bragg peak position for a given plane (hkl). Due to the large atomic form factor of Ba, there are no (hkl) conditions for which the structure factor F_{hkl} disappears. In addition, according to formula (3), the lower order peaks at low θ_{hkl} show a relatively large L.P. factor value, giving larger diffraction intensity. Therefore, all reflections of stoichiometric BTO should be clearly observable. For sample A, however, with 90% excessive [Ti], the 3 lowest-ordered Bragg's peaks: $(001)_{BTO}$, $(101)_{BTO}$, and $(111)_{BTO}$ are missing in the RHEED patterns (Figure 1) as well as in the XRD (Figure 2) and TEM (Figure 5) figures, indicating the extra [Ti] results in a unique diffraction phenomenon. To understand this, we consider the Ba_xTiO_z compound with Ba composition x from 0 to 1, and oxygen content z from 0 to $2+x$, assuming charge neutrality. We further assume the atomic form factor of deficient [Ba] and oxygen can be expressed by xf_{Ba} and $zf_O/3$, respectively. Then, combining formula 1 with 3, taking into account those non-stoichiometric atomic form factors, the diffraction intensity for each plane (hkl) can be derived. In order to see how the stoichiometry influences the diffraction pattern, we evaluate again the intensity ratio of the 3 lowest-ordered peaks with respect to the (002) peak, in functions of various x and z compositions. Afterwards, the intensity ratios $I_{(001)}/I_{(002)}$, $I_{(101)}/I_{(002)}$, and $I_{(111)}/I_{(002)}$ for Ba_xTiO_z are normalized to those for stoichiometric $BaTiO_3$ and color-mapped in Figures 6(a)–6(c), respectively. The black solid lines in each mapping show the [Ba]/[Ti] ratio measured using RBS. Any colors other than the deep red in the color bar define a composition of Ba_xTiO_z with the smaller diffraction intensity ratio than that for stoichiometric $BaTiO_3$, which is the unique phenomenon that we are interested in. Figures 6(a)–6(c) show the windows of Ba_xTiO_z having smaller $(001)_{BTO}$, $(101)_{BTO}$, and $(111)_{BTO}$ diffraction intensity than that for the stoichiometric BTO, respectively. In order to describe the diffraction behavior observed in sample A for which the $(001)_{BTO}$, $(101)_{BTO}$, and $(111)_{BTO}$ Bragg peaks are unobservable, Figure 6(d) defines the area where the 3 composition windows of Figures 6(a)–6(c) overlap. The resulting triangular region shows that sample A is not only Ti-rich but also oxygen-deficient. From RBS, we found a [Ba] deficiency of −90% for sample A, which is beyond the lower bound of the triangular area (−80%). Yet, from the XRD-data shown in Figure 2, we know that some poly-titanate compounds formed in sample A and precipitated in the grain boundaries of twinned $(111)_{BTO}$, evidenced by multi-peaks in the $\omega-2\theta$ scan of the $(101)_{BTO}$ and $(111)_{BTO}$ planes. Therefore, we can infer that more than 10% [Ti] is not incorporated in the BTO lattice but forms a poly-titanate. Besides, the lattice expansion observed in Figure 4 indicates that plenty of V_o exists in sample A, in agreement with Figure 6(d). This explains the disappearance of the 3 lowest-ordered Bragg peaks for sample A, as observed in our diffraction analysis.

To describe the Ba-rich samples, we use $BaTi_yO_z$ as our model, where y ranges from 0 to 1 and z from 0 to $2+y$. Similar to the Ti-rich case, we assume the atomic form

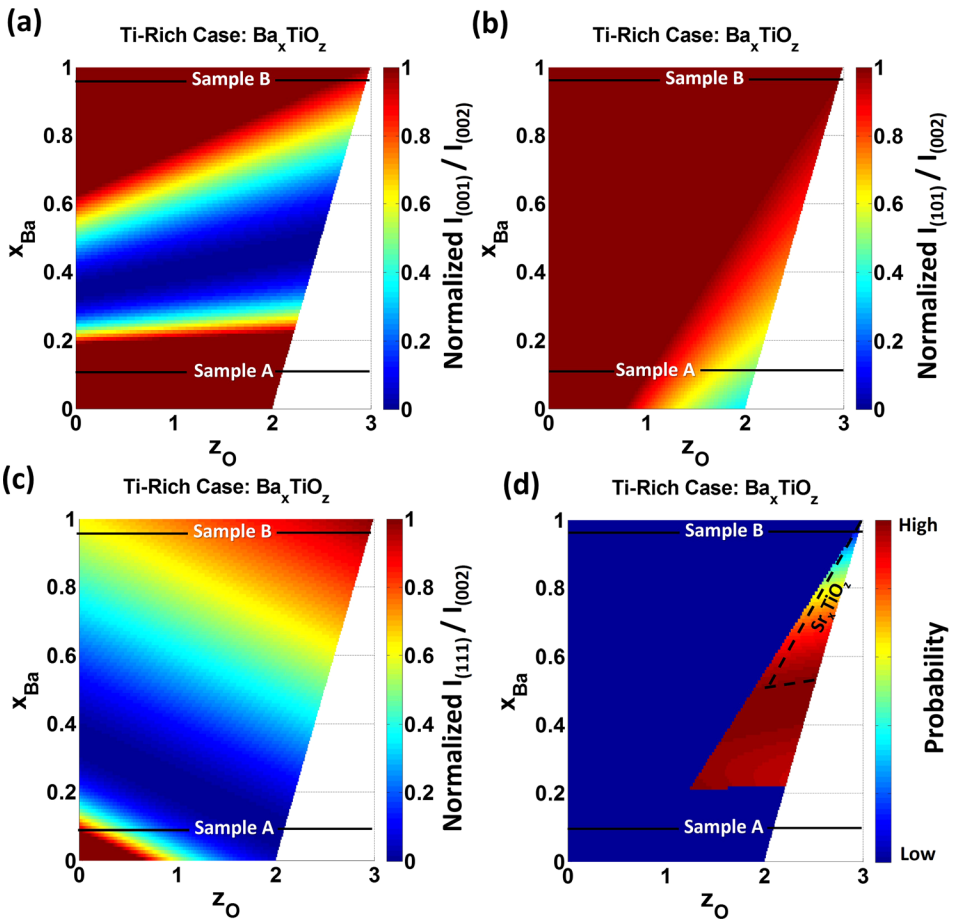

FIG. 6. The calculated mappings of (a) $I_{(001)}/I_{(002)}$,(b) $I_{(101)}/I_{(002)}$, and (c) $I_{(111)}/I_{(002)}$ for the Ti-rich compound Ba_xTiO_z, which are normalized by those ratios for the stoichiometric $BaTiO_3$. (d) The probability distribution for having lower $I_{(001)}/I_{(002)}$, $I_{(101)}/I_{(002)}$, and $I_{(111)}/I_{(002)}$ at the same time. The RBS-measured [Ba]/[Ti] ratios for samples A and B are denoted by the solid lines on all mappings. The Ti-rich STO case is indicated by the black dashed lines in (d).

factors of deficient [Ti] and oxygen are expressed by yf_{Ti} and $zf_O/3$, respectively. Then, the normalized diffraction efficiencies $I_{(001)}/I_{(002)}$, $I_{(101)}/I_{(002)}$, and $I_{(111)}/I_{(002)}$ can be evaluated as illustrated in Figures 7(a)–7(c), respectively. The RBS-measured [Ba]/[Ti] ratios are indicated by the black solid line in these figures. Different from the Ti-rich case, in the Ba-excess case, no combination of y and z leads to a decrease in the intensity of the $(001)_{BTO}$ and $(101)_{BTO}$ peaks. Yet, there is still a small region with an excess [Ba] between 0% and 30% and with some V_o which shows a lower $I_{(111)}/I_{(002)}$ than that for the stoichiometric BTO, as visible in Figure 7(c). Combined with the $I_{(001)}/I_{(002)}$, $I_{(101)}/I_{(002)}$, and $I_{(111)}/I_{(002)}$ mappings, however, there is no overlapping region where all 3 peaks disappear at the same time, as can be seen from Figure 7(d).

Comparing the experimental results of Figure 3 and the modelling results presented in Figures 6 and 7, the trend of the relative diffraction efficiencies $I_{(001)}/I_{(002)}$, $I_{(101)}/I_{(002)}$, and $I_{(111)}/I_{(002)}$ with stoichiometry can be further discussed. In Figure 3, $I_{(001)}/I_{(002)}$, $I_{(101)}/I_{(002)}$, and $I_{(111)}/I_{(002)}$ are all decreasing with more [Ti] being incorporated inside the BTO layer. This is in agreement with the triangular region delineated for the Ti-rich case in Figure 6(d): excess [Ti] and oxygen deficiency in the BTO layer can lead to an intensity degradation of diffraction at the $(001)_{BTO}$, $(101)_{BTO}$, and $(111)_{BTO}$ planes. On the other hand, for the Ba-rich case (Figure 7), the calculated diffraction efficiencies $I_{(001)}/I_{(002)}$ and $I_{(101)}/I_{(002)}$ color red, indicating that both should increase with increasing [Ba]. This is in agreement with the experiments for $I_{(001)}/I_{(002)}$ but not for $I_{(101)}/I_{(002)}$ in the whole case, which, as can be seen from Figure 3, with increasing the [Ba] content from −4% (sample B) to 8% (sample C), increases. This disagreement might result from the calculation which does not take the setup geometry into account. Figure 7(c) shows a triangular region defining the Ba-rich, oxygen-deficient composition window, where the relative diffraction efficiency $I_{(111)}/I_{(002)}$ is smaller than that for stoichiometric BTO. With further increasing [Ba], the ratio $I_{(111)}/I_{(002)}$ will increase again and become larger than for stoichiometric BTO. This trend matches well with the experimental trend seen comparing samples C and D in Figure 3. Therefore, at least qualitatively, the diffraction models we propose for both Ti- and Ba-rich BTO can explain the experimentally observed phenomena very well.

Interestingly, within the wide literature on STO, and even though STO has the same perovskite crystal structure as BTO, to our knowledge, there is no report of a diffraction behavior similar to what we describe in this work. Since Sr^{2+} (36) has less electrons than Ba^{2+}(54), the atomic form factor of Sr is also smaller than that of Ba. Therefore, Sr^{2+} in an STO-film cannot exhibit such a large electron or X-ray scattering as Ba. Therefore, compared to Ti-rich BTO, the composition window for Ti-rich STO has the 3 lowest-ordered Bragg peaks missing simultaneously shrinks, as indicated by the dashed lines in Figure 6(d). Therefore, this unique diffraction phenomenon becomes comparatively

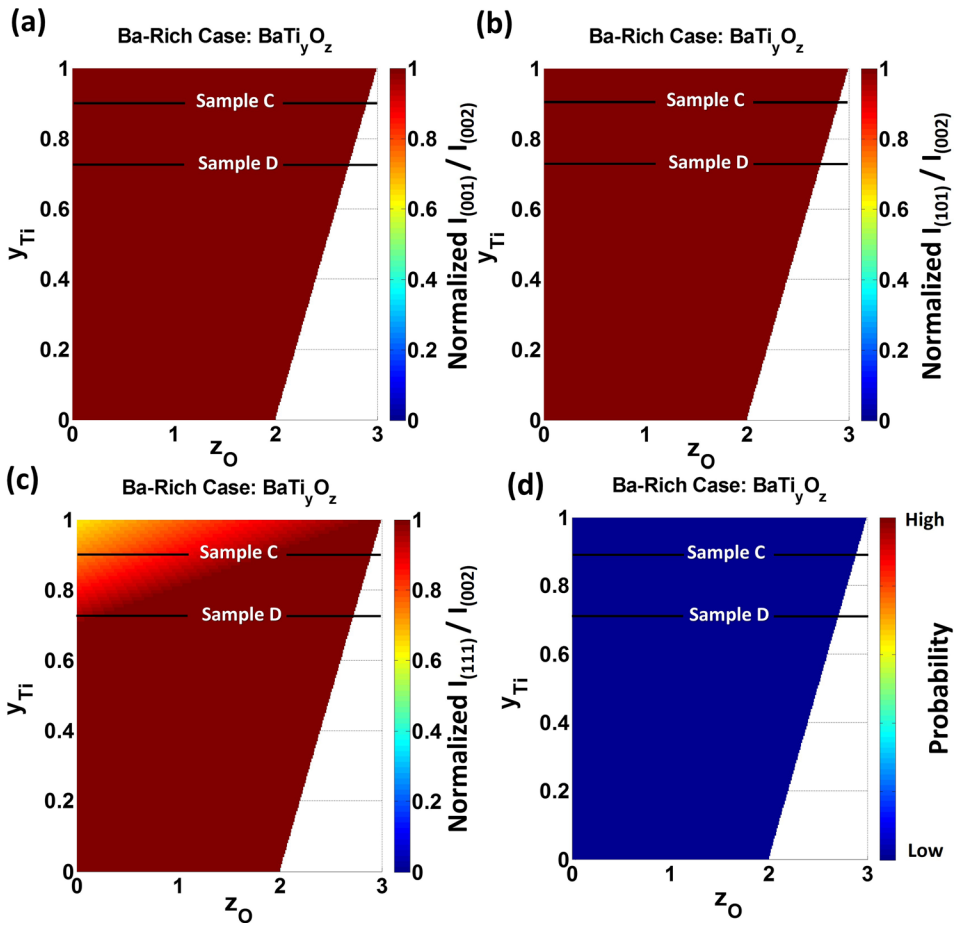

FIG. 7. The calculated mappings of (a) $I_{(001)}/I_{(002)}$,(b) $I_{(101)}/I_{(002)}$, and (c) $I_{(111)}/I_{(002)}$ for the Ba-rich compound $BaTi_yO_z$, which are normalized by those ratios for the stoichiometric $BaTiO_3$. (d) The probability distribution for having lower $I_{(001)}/I_{(002)}$, $I_{(101)}/I_{(002)}$, and $I_{(111)}/I_{(002)}$, at the same time. The RBS-measured [Ba]/[Ti] ratios for samples C and D are denoted by the solid lines on all mappings.

more difficult to be observed in STO-films. For that reason, Sr-rich STO behaves similar to Ba-rich BTO, and equally does not exhibit a composition window where all 3 lowest-ordered peaks disappear.

V. CONCLUSION

In this work, we utilized RBS to measure the exact [Ba]/[Ti] ratio in BTO-films and developed diffraction models to understand the effect of the precise stoichiometry on the diffraction phenomenon observed in RHEED, XRD, and TEM diffraction studies. In the RHEED patterns, non-stoichiometric BTO does not show $\times 2$ surface reconstructions along the $[100]_{BTO}$ and $[110]_{BTO}$ directions, presumably because the [Ba]/[Ti] ratio is too far away from unit in these layers. However, we observe that excess [Ba] and [Ti] in the non-stoichiometric BTO-layers generates twinning planes and induces a rougher surface, as revealed in the RHEED patterns. Besides, excess [Ti] is observed to change the BTO diffraction behavior, making the ± 1st-ordered RHEED lines along the $[100]_{BTO}$ and $[110]_{BTO}$ directions disappear. Further, despite we considered a very broad range of [Ba]/[Ti] ratios, all samples still show a four-fold tetragonal symmetry in the crystal structure. Additionally, we found that the $\omega - 2\theta$ scan along $[001]_{BTO}$ does not provide sufficient information to judge if a given BTO layer is single-crystalline and stoichiometric. The non-stoichiometric BTO samples show poly-crystalline-like diffraction patterns, which might result from any non-stoichiometric compound precipitation. In addition, evaluated from $\omega - 2\theta$ scans, the out-of-plane lattice constant $a_{\perp}$ for BTO follows a similar trend as function of the stoichiometry as STO, having a local minimum for the composition [Ba]/[Ti] around 1. On the other hand, the variation of $a_{\parallel}$ as a function of the layer stoichiometry shows a completely different behavior: it is decreasing with more [Ba] inside the layer. Therefore, adjusting the ratio [Ba]/[Ti] offers a route to adjust the BTO tetragonality and hence to control the ferroelectricity of the BTO layer for device applications. In addition, the 3 lowest-ordered Bragg peak relative intensity ratios $I_{(001)}/I_{(002)}$, $I_{(101)}/I_{(002)}$, and $I_{(111)}/I_{(002)}$ derived from the $\omega - 2\theta$ scan depend on BTO stoichiometry in a characteristic way. Compared with the intensity ratios of stoichiometric BTO, extra [Ti] will decrease all three ratios $I_{(001)}/I_{(002)}$, $I_{(101)}/I_{(002)}$ and $I_{(111)}/I_{(002)}$ simultaneously, making the 3 lowest-ordered Bragg peaks unobservable for sample A (with the highest excess [Ti]). This peak disappearance is also in good agreement with the RHEED and SAED patterns for sample A. On the other hand, for Ba-rich BTO, the ratios of $I_{(001)}/I_{(002)}$, $I_{(101)}/I_{(002)}$, and $I_{(111)}/I_{002}$ are not all increasing. To understand this, we proposed a model that explains how excess [Ba] or [Ti] in non-stoichiometric BTO layers indeed induces different experimental diffraction behaviors from the stoichiometric layer. Therefore, this work provides insight and better understanding in how the stoichiometry of a BTO layer influences different diffraction phenomena, thereby assisting in precisely controlling the properties of a BTO-layer for given applications.

ACKNOWLEDGMENTS

The authors thank the hardware maintenance of our MBE systems from Hans Costermans and Kevin Dubois.

[1]R. Guo, Z. Wang, S. Zheng, K. Han, L. Huang, D. G. Schlom, T. Venkatesan, J. Ariando, and J. Chen, Sci. Rep. **5**, 12576 (2015).
[2]C. Xiong, W. H. P. Pernice, J. H. Ngai, J. W. Reiner, D. Kumah, F. J. Walker, C. H. Ahn, and H. X. Tang, Nano Lett. **14**, 1419 (2014).
[3]S. H. Baek, J. Park, D. M. Kim, V. A. Aksyuk, R. R. Das, S. D. Bu, D. A. Felker, J. Lettieri, V. Vaithyanathan, S. S. N. Bharadwaja, N. Bassiri-Gharb, Y. B. Chen, H. P. Sun, C. M. Folkman, H. W. Jang, D. J. Kreft, S. K. Streiffer, R. Ramesh, X. Q. Pan, S. Trolier-McKinstry, D. G. Schlom, M. S. Rzchowski, R. H. Blick, and C. B. Eom, Science **334**, 958 (2011).
[4]D. G. Schlom, L.-Q. Chen, X. Pan, A. Schmehl, and M. A. Zurbuchen, J. Am. Ceram. Soc. **91**, 2429 (2008).
[5]A. A. Demkov and A. B. Posadas, *Integration of Functional Oxides With Semiconductors* (Springer, New York, Heidelberg, Dordrecht, London, 2014).
[6]J. W. Reiner, A. M. Kolpak, Y. Segal, K. F. Garrity, S. Ismail Beigi, C. H. Ahn, F. J. Walker, S. Ismail-Beigi, C. H. Ahn, and F. J. Walker, Adv. Mater. **22**, 2919 (2010).
[7]R. McKee, F. Walker, and M. Chisholm, Phys. Rev. Lett. **81**, 3014 (1998).
[8]H. L. Yu, Y. Z. Wu, X. F. Jiang, M. Q. Cai, L. P. Gu, and G. W. Yang, J. Appl. Phys. **114**, 173502 (2013).
[9]A. Kalabukhov, R. Gunnarsson, J. Börjesson, E. Olsson, T. Claeson, and D. Winkler, Phys. Rev. B **75**, 121404 (2007).
[10]L. Ji, M. D. McDaniel, S. Wang, A. B. Posadas, X. Li, H. Huang, J. C. Lee, A. A. Demkov, A. J. Bard, J. G. Ekerdt, and E. T. Yu, Nat. Nanotechnol. **10**, 84 (2014).
[11]F. S. Aguirre-Tostado, A. Herrera-Gómez, J. C. Woicik, R. Droopad, Z. Yu, D. G. Schlom, P. Zschack, E. Karapetrova, P. Pianetta, and C. S. Hellberg, Phys. Rev. B **70**, 201403 (2004).
[12]A. M. Kolpak and S. Ismail-Beigi, Phys. Rev. B **83**, 165318 (2011).
[13]C. J. Fennie and K. M. Rabe, Phys. Rev. B **68**, 184111 (2003).
[14]Y. Y. Guo, H. M. Liu, D. P. Yu, and J.-M. Liu, Phys. Rev. B **85**, 104108 (2012).
[15]C. Dubourdieu, H. Roussel, C. Jimenez, M. Audier, J. P. Sénateur, S. Lhostis, L. Auvray, F. Ducroquet, B. J. O'Sullivan, P. K. Hurley, S. Rushworth, and L. Hubert-Pfalzgraf, Mater. Sci. Eng. B **118**, 105 (2005).
[16]M. Vehkamäki, T. Hänninen, M. Ritala, M. Leskelä, T. Sajavaara, E. Rauhala, and J. Keinonen, Chem. Vap. Deposition **7**, 75 (2001).
[17]M. D. McDaniel, A. Posadas, T. Q. Ngo, A. Dhamdhere, D. J. Smith, A. A. Demkov, and J. G. Ekerdt, J. Vac. Sci. Technol. A **31**, 01A136 (2013).
[18]P. Fisher, H. Du, M. Skowronski, P. A. Salvador, O. Maksimov, and X. Weng, J. Appl. Phys. **103**, 013519 (2008).
[19]C. M. Brooks, L. F. Kourkoutis, T. Heeg, J. Schubert, D. A. Muller, and D. G. Schlom, Appl. Phys. Lett. **94**, 162905 (2009).
[20]Z. Yu, Y. Liang, C. Overgaard, X. Hu, J. Curless, H. Li, Y. Wei, B. Craigo, D. Jordan, R. Droopad, J. Finder, K. Eisenbeiser, D. Marshall, K. Moore, J. Kulik, and P. Fejes, Thin Solid Films **462–463**, 51 (2004).
[21]J. M. LeBeau, R. Engel-Herbert, B. Jalan, J. Cagnon, P. Moetakef, S. Stemmer, and G. B. Stephenson, Appl. Phys. Lett. **95**, 142905 (2009).
[22]B. Fultz and J. Howe, *Transmission Electron Microscopy and Diffractometry of Materials* (Springer-Verlag, Berlin, Heidelberg, 2013), Chap. 1.
[23]E. Heymann and H. Bloom, Nature **156**, 479 (1945).
[24]J. B. Murgatroyd and R. F. Sykes, Nature **156**, 716 (1945).
[25]S. Abel, T. Stöferle, C. Marchiori, C. Rossel, M. D. Rossell, R. Erni, D. Caimi, M. Sousa, A. Chelnokov, B. J. Offrein, and J. Fompeyrine, Nat. Commun. **4**, 1671 (2013).
[26]T. Suzuki, Y. Nishi, and M. Fujimoto, J. Am. Ceram. Soc. **83**, 3185 (2000).
[27]G. Y. Yang, G. D. Lian, E. C. Dickey, C. A. Randall, D. E. Barber, P. Pinceloup, M. A. Henderson, R. A. Hill, J. J. Beeson, and D. J. Skamser, J. Appl. Phys. **96**, 7500 (2004).
[28]A. Lotnyk, A. Graff, S. Senz, N. D. Zakharov, and D. Hesse, Solid State Sci. **10**, 702 (2008).

[29]C. Merckling, G. Saint-Girons, C. Botella, G. Hollinger, M. Heyns, J. Dekoster, and M. Caymax, Appl. Phys. Lett. **98**, 092901 (2011).
[30]J. L. Wang, J. Leroy, G. Niu, G. Saint-Girons, B. Gautier, B. Vilquin, and N. Barrett, Chem. Phys. Lett. **592**, 206 (2014).
[31]Y. L. Zhu, M. J. Zhuo, X. L. Ma, and H. B. Lu, Mater. Lett. **61**, 1971–1973 (2007).
[32]T. Suzuki, Y. Nishi, and M. Fujimoto, Philos. Mag. A **80**, 621 (2000).
[33]K. Shimoyama, K. Kubo, M. Lida, and K. Yamabe, J. Vac. Sci. Technol. A **19**, 2083 (2001).
[34]S. Abel, Ph.D. thesis (Universite Grenoble Alpes, 2014).
[35]M. Yashima, R. Tu, T. Goto, and H. Yamane, Appl. Phys. Lett. **87**, 101909 (2005).
[36]J. Bland, Acta Crystallogr. **14**, 875 (1961).
[37]S. Stemmer, S. K. Streiffer, N. D. Browning, and A. I. Kingon, Appl. Phys. Lett. **74**, 2432 (1999).
[38]Y. He, Thermochim. Acta **419**, 135 (2004).
[39]D. F. Gibbons, Phys. Rev. **112**, 136 (1958).
[40]G. Delhaye, C. Merckling, M. El-Kazzi, G. Saint-Girons, M. Gendry, Y. Robach, G. Hollinger, L. Largeau, and G. Patriarche, J. Appl. Phys. **100**, 124109 (2006).
[41]S. Sakai and M. Takahashi, Materials **3**, 4950 (2010).